Unique hollow heterostructured $CdS/Cd_{0.5}Zn_{0.5}S\text{-}Mo_{1-x}W_xS_2$: Highly-improved visible-light-driven H_2 generation via synergy of $Cd_{0.5}Zn_{0.5}S$ protective shell and defect-rich $Mo_{1-x}W_xS_2$ cocatalyst

Wenjing Wang[1], Hanchu Chen[1,3], Jiakun Wu[1], Hui Wang[3], Shaoxiang Li[2], Bo Wang[4], Yanyan Li[1], Haifeng Lin[1,5] (✉), and Lei Wang[1,2] (✉)

[1] Key Laboratory of Eco-chemical Engineering, Key Laboratory of Optic-electric Sensing and Analytical Chemistry of Life Science, Shandong Provincial Key Laboratory of Olefin Catalysis and Polymerization, Taishan Scholar Advantage and Characteristic Discipline Team of Eco-Chemical Process and Technology, College of Chemistry and Molecular Engineering, Qingdao University of Science and Technology, Qingdao 266042, China

[2] Shandong Engineering Research Center for Marine Environment Corrosion and Safety Protection, College of Environment and Safety Engineering, Qingdao University of Science and Technology, Qingdao 266042, China

[3] Shandong Provincial Key Laboratory of Olefin Catalysis and Polymerization, Key Laboratory of Rubber-Plastics of Ministry of Education, School of Polymer Science and Engineering, Qingdao University of Science and Technology, Qingdao 266042, China

[4] School of Applied Physics and Materials, Wuyi University, Jiangmen 529020, China

[5] State Key Laboratory of Inorganic Synthesis and Preparative Chemistry, College of Chemistry, Jilin University, Changchun 130012, China

ABSTRACT

Photocatalytic water splitting for hydrogen (H_2) production is a green sustainable technology, in which highly-efficient steady photocatalysts are fundamentally required. In this work, unique $CdS/Cd_{0.5}Zn_{0.5}S\text{-}Mo_{1-x}W_xS_2$ photocatalyst constructed by CdS hollow nano-spheres with successively surface-modified $Cd_{0.5}Zn_{0.5}S$ shell and defect-rich $Mo_{1-x}W_xS_2$ ultrathin nanosheets was reported for the first time. Interestingly, the $Cd_{0.5}Zn_{0.5}S$ shell could greatly enhance the photo-stability and reduce the carrier recombination of CdS. Meanwhile, enriching active sites and accelerating charge transfer could be achieved via anchoring defect-rich $Mo_{1-x}W_xS_2$ onto $CdS/Cd_{0.5}Zn_{0.5}S$ hollow heterostructures. Specifically, the optimized $CdS/Cd_{0.5}Zn_{0.5}S\text{-}Mo_{1-x}W_xS_2$ (6 h $Cd_{0.5}Zn_{0.5}S$-coating, 7 wt.% $Mo_{1-x}W_xS_2$, $x = 0.5$) hybrid delivered an exceptional H_2 generation rate of 215.99 mmol·g^{-1}·h^{-1}, which is approximately 502, 134, and 23 times that of pure CdS, $CdS/Cd_{0.5}Zn_{0.5}S$, and 3 wt.% Pt-loaded $CdS/Cd_{0.5}Zn_{0.5}S$, respectively. Remarkably, a high H_2 evolution reaction (HER) apparent quantum yield (AQY) of 64.81% was obtained under 420-nm irradiation. In addition, the $CdS/Cd_{0.5}Zn_{0.5}S\text{-}Mo_{1-x}W_xS_2$ was also durable for H_2 production under long-term irradiation. This work provides valuable inspirations to rational design and synthesis of efficient and stable hybrid photocatalysts for solar energy conversion.

KEYWORDS

CdS hollow nano-spheres, $Cd_{0.5}Zn_{0.5}S$ protective shells, defect-rich $Mo_{1-x}W_xS_2$ nanosheets, cocatalysts, photocatalytic H_2 evolution

1   Introduction

With the depletion of traditional fossil fuels in these years, the renewable hydrogen energy has aroused considerable interest as an ideal alternative due to its high energy-density and clean combustion product [1, 2]. Among various approaches to produce hydrogen, photocatalytic water-splitting in the presence of semiconductors is regarded as one of the most promising ways because it can directly transform the inexhaustible solar energy into chemical energy [3–5]. So far, diverse semiconductors like metal oxides [6, 7], metal sulfides [8–10], and polymers [11–13], have been explored for H_2 evolution reaction (HER), since the first discovery of photoelectrocatalytic water-splitting over TiO_2 electrode by Honda and Fujishima in 1972 [14]. Particularly, cadmium sulfide (CdS) has drawn great attention for photocatalysis owing to its superior light-absorption capacity as well as suitable band-edge positions for water splitting [15]. Considering the significant structure–activity correlation in heterogeneous photocatalysis, great research efforts have been concentrated on morphological and structural manipulation of CdS in order to obtain an outstanding photocatalytic capability [16–18].

In view of the distinct advantages of semiconductor hollow nanostructures for photocatalysis [19–21], for instance, enhanced light harvesting enabled by multiple reflections and scattering within the hollow cavity, boosted charge separation due to the reduced migration distance of photogenerated carriers, as well as facilitated permeation and diffusion of reactants through the voids between constituent nanoparticles, CdS hollow architectures like nanotubes [22], hollow spheres [23], hollow polyhedrons [24], etc. have recently been synthesized for photocatalytic reactions. Nevertheless, bare CdS hollow

nanostructures are still afflicted with the drawbacks of instability caused by photocorrosion and charge recombination originating from the abundant surface defects [25], which give rise to an inferior photo-activity. An effective strategy to conquer these two issues is to construct a wider-bandgap semiconductor as the protective shell for CdS nanocrystals [25, 26], by which the surface trap states can be passivated and the CdS nanocrystals could be physically separated from their surrounding medium [27], leading to dramatically enhanced photo-stability and reduced recombination of charge carriers. However, the strategy mentioned above is usually implemented with the core–shell systems but rarely applied for the hollow nanostructures. Due to their similar crystalline structure and lattice constants to CdS, the Zn-doped CdS such as $Cd_{0.5}Zn_{0.5}S$ with an increased bandgap than CdS are suitable to function as the surface protection layer for CdS hollow nanostructures. In addition, coupling the photocatalyst with cocatalysts has been demonstrated to be a quite valid approach to promote charge separation through the cocatalyst/semiconductor heterojunctions and accelerate surface catalytic reactions by providing abundant active sites to decrease the reaction activation energy [28, 29]. Of late, layered transition metal chalcogenides, especially MoS_2, has been considered as a noble-metal-alternative cocatalyst for photocatalytic H_2 evolution [30], because of its near zero free energy of H adsorption for HER analogous to Pt-like catalyst [31]. However, the poor electrical conductivity of MoS_2 and limited active sites on the exposed edges restrict its cocatalytic HER activity significantly [32]. Recent investigations manifest that the catalytic activity of MoS_2 can be promoted by chemical doping of O [33], N [34], P [35], etc., which contribute to the increased conductivity and active-site amount. Besides, Shi et al. found that tuning the energy level of MoS_2 to match HER via transition-metal doping is a promising way to improve its catalytic performance [36]. Moreover, the heteroatoms doped in MoS_2 will modulate the electronic density and activity of adjacent Mo and S atoms and lots of active sites can thus be generated in the basal planes of MoS_2 nanosheets [36]. On the other hand, more additional HER active edge sites can be created for MoS_2 by the introduction of structural defects [37]. It is well known that the valence state and ionic radius of W are close to that of Mo. Additionally, the WS_2 has a higher intrinsic electrical conductivity than MoS_2 [38, 39]. Therefore, it is anticipated that the conductivity of MoS_2 and its active-site number can be increased by W-doping, and the defect-rich $Mo_{1-x}W_xS_2$ ultrathin nanosheets would be a highly efficient cocatalyst for photocatalytic H_2 evolution, although the relevant studies have rarely been reported to now.

In this work, unique $CdS/Cd_{0.5}Zn_{0.5}S$-$Mo_{1-x}W_xS_2$ hybrid hollow nano-spheres were designed and prepared for the first time, which consist of $CdS/Cd_{0.5}Zn_{0.5}S$ hollow nano-spheres obtained by a template-assisted ultrasonic water-bath process as photo-absorber and the defect-rich $Mo_{1-x}W_xS_2$ ultrathin nanosheets produced from a novel solvothermal method as cocatalyst. Under visible-light irradiation, the $CdS/Cd_{0.5}Zn_{0.5}S$-$Mo_{1-x}W_xS_2$ composites displayed an outstanding HER capability due to the excellent light harvest benefiting from the $CdS/Cd_{0.5}Zn_{0.5}S$-$Mo_{1-x}W_xS_2$ hollow nanostructure, the existence of abundant active sites in the defective $Mo_{1-x}W_xS_2$ cocatalyst, as well as the efficient spatial charge separation through the interfacial heterojunctions. Moreover, it is interesting to find that the cocatalytic HER activity of $Mo_{1-x}W_xS_2$ over $CdS/Cd_{0.5}Zn_{0.5}S$ hollow nano-spheres is dramatically improved as compared with that of pristine MoS_2 and WS_2 counterparts. The success of rational structural modulation toward exceptional HER property here will facilitate the development of high-

performance photocatalysts for sustainable solar conversion and utilization.

2 Experimental

2.1 Materials

All chemicals (analytical grade) including tetraethyl orthosilicate (TEOS), $CdCl_2\cdot4H_2O$, $ZnCl_2$, $C_6H_5Na_3O_7\cdot2H_2O$, WCl_4, $(NH_4)_2MoS_4$, $Na_2S\cdot9H_2O$, Na_2SO_3, triethanolamine (TEOA), N,N-dimethylacetamide (DMF), ammonia, thioacetamide, lactic acid, and ethanol were purchased from Sinopharm Chemical Reagent, Co., Ltd. (Shanghai, China) and were used as received in this work without further purification.

2.2 Synthesis of SiO_2 spheres

Silica spheres were prepared by a modified Stöber method. Typically, 3.14 mL ammonia (28%) was mixed with 74 mL ethanol and 10 mL deionized water to form a homogeneous solution after stirring for 0.5 h. Subsequently, 6 mL TEOS was dropwise added into the above solution to perform the hydrolysis reaction under agitation condition. After stirring at room temperature for 6 h, the resultant SiO_2 spheres were rinsed by centrifugation with deionized water and ethanol for three times, and dried in an oven at 60 °C for 12 h.

2.3 Synthesis of SiO_2/CdS core–shell nano-spheres

SiO_2/CdS core–shell nano-spheres were synthesized by an ultrasound-assisted water-bath method. In a typical synthesis, 0.3 g SiO_2 spheres were dispersed into 30 mL deionized water under stirring condition. After that, 20 mL of 0.1 M $C_6H_5Na_3O_7\cdot2H_2O$, 15 mL of 0.1 M $CdCl_2\cdot2.5H_2O$, and 30 mL of 0.1 M CH_4N_2S were added to the SiO_2 suspension in sequence. After stirring for 30 min, 3 mL of $NH_3\cdot H_2O$ (25%) was added, and the obtained mixed solution was heated in 65 °C water-bath for 70 min under ultrasonic condition. Unless otherwise specified, the reaction time for CdS-coating defaults to 70 min. After reaction, the product was washed three times with deionized water and ethanol, centrifuged, and dried at 70 °C for 6 h in a vacuum drying oven. For comparison, CdS solid nano-spheres were prepared after ultrasonic water-bath reaction for 6 h according to the above procedures except the use of SiO_2 template.

2.4 Synthesis of SiO_2/CdS/$Cd_{0.5}Zn_{0.5}S$ nano-spheres

The as-prepared SiO_2/CdS nano-spheres were evenly dispersed in 285 mL of deionized water, then 20 mL of 0.1 M $C_6H_5Na_3O_7\cdot2H_2O$, 15 mL of 0.05 M $CdCl_2\cdot2.5 H_2O$, 15 mL of 0.05 M $ZnCl_2$, and 30 mL of 0.1 M CH_4N_2S were added in sequence. After stirring for 30 min, 3 mL of $NH_3\cdot H_2O$ (25%) was added, and this mixed solution was heated in 50 °C water-bath for 6 h under ultrasonic condition to get the SiO_2/CdS/$Cd_{0.5}Zn_{0.5}S$ nano-spheres. Unless otherwise specified, the reaction time for $Cd_{0.5}Zn_{0.5}S$-coating defaults to 6 h. For comparison, $Cd_{0.5}Zn_{0.5}S$ solid nano-spheres were also fabricated with the above synthesis strategy except the addition of SiO_2/CdS nano-spheres.

2.5 Synthesis of CdS and CdS/$Cd_{0.5}Zn_{0.5}S$ hollow nano-spheres

Firstly, the as-prepared SiO_2/CdS or SiO_2/CdS/$Cd_{0.5}Zn_{0.5}S$ samples were placed into a tube furnace and heated to 350 °C with a heating rate of 5 °C/min under N_2 atmosphere, and kept at 350 °C for 2 h, then cooled to room temperature naturally. After that, 0.2 g of the calcined sample was dispersed in 10 mL ethanol, and then etched with 5 wt.% hydrofluoric acid (HF) for 40 min under stirring condition to obtain the uniform CdS

and CdS/Cd$_{0.5}$Zn$_{0.5}$S hollow nano-spheres.

2.6 Synthesis of MoS$_2$, WS$_2$, and Mo$_{1-x}$W$_x$S$_2$ nanosheets

The Mo$_{1-x}$W$_x$S$_2$ nanosheets were synthesized by a solvothermal method. Typically, 200 mg of (NH$_4$)$_2$MoS$_4$ was dispersed in 30 mL DMF, into which WCl$_4$ with different molar ratios to (NH$_4$)$_2$MoS$_4$ was added subsequently. Then the obtained homogeneous solution was transferred to a 30 mL Teflon-lined autoclave and heated at 200 °C for 10 h. After being naturally cooled, the product was washed thrice with ethanol and water, centrifuged, and dried in a vacuum oven at 70 °C for 5 h. The synthesized product was labeled as Mo$_{1-x}$W$_x$S$_2$ (x = 0.1, 0.3, 0.5, 0.7, and 0.9), where x represents the molar concentration of W element. Pure MoS$_2$ nanosheets were synthesized according to the above procedure but without the addition of WCl$_4$. Similarly, WS$_2$ nanosheets can be produced when 1 mmol WCl$_4$ and 6 mmol thioacetamide were employed as the W and S sources, respectively.

2.7 Synthesis of CdS/Cd$_{0.5}$Zn$_{0.5}$S-MoS$_2$, CdS/Cd$_{0.5}$Zn$_{0.5}$S-WS$_2$, and CdS/Cd$_{0.5}$Zn$_{0.5}$S-Mo$_{1-x}$W$_x$S$_2$ hybrid hollow nano-spheres

Specifically, a certain amount of MoS$_2$, WS$_2$, or Mo$_{1-x}$W$_x$S$_2$ nanosheets were added to a round-bottomed flask containing 35 mL of N, N-dimethylformamide, which were subsequently treated by sonication for 3 h to form a homogeneous suspension. Following this step, 50 mg of CdS/Cd$_{0.5}$Zn$_{0.5}$S hollow nano-spheres were mingled with the above exfoliated MoS$_2$, WS$_2$, or Mo$_{1-x}$W$_x$S$_2$ nanosheets through sonication for 15 min, and then this mixture was sealed and stirred for 12 h to complete the adsorption and assembly processes. After centrifugal washing with deionized water and ethanol, the product was dried in a vacuum oven at 70 °C for 6 h to form the CdS/Cd$_{0.5}$Zn$_{0.5}$S-MoS$_2$, CdS/Cd$_{0.5}$Zn$_{0.5}$S-WS$_2$, or CdS/Cd$_{0.5}$Zn$_{0.5}$S-Mo$_{1-x}$W$_x$S$_2$ hybrids. For simplicity, the CdS/Cd$_{0.5}$Zn$_{0.5}$S-MoS$_2$, CdS/Cd$_{0.5}$Zn$_{0.5}$S-WS$_2$, and CdS/Cd$_{0.5}$Zn$_{0.5}$S-Mo$_{1-x}$W$_x$S$_2$ composites were abbreviated as CS/CZ$_{0.5}$S-yMS, CS/CZ$_{0.5}$S-yWS, and CS/CZ$_{0.5}$S-yMW$_x$S, where y stands for the mass percentage of MoS$_2$, WS$_2$, and Mo$_{1-x}$W$_x$S$_2$ multiplied by 100, respectively.

2.8 Characterizations

The X-ray diffraction (XRD) data were collected by a Rigaku D/max 2500 PC X-ray diffractometer using monochromatic Cu Kα radiation (40 kV, 150 mA). The ultraviolet–visible (UV–vis) absorption spectra were recorded on a Shimadzu UV 3600 spectrometer equipped with an integrating sphere accessory. Scanning electron microscopy (SEM) observations were carried out with a ZEISS Merlin compact scanning electron microscope. Transmission electron microscopy (TEM), high-resolution TEM (HRTEM), dark-field scanning transmission electron microscopy (STEM), and energy dispersive X-ray spectroscopy (EDX) mapping measurements were performed on a JEOL JEM-2100F transmission electron microscope. The elementary composition of photocatalysts was determined by EDX test. The Raman signals were detected with a LabRAM HR Evolution Raman spectrometer using a laser wavelength of 532 nm. Electron paramagnetic resonance (EPR) data were obtained by a Bruker A300 spectrometer operating at 113 K. X-ray photoelectron spectroscopy (XPS) tests were completed on a Thermo Fisher ESCALAB 250 Xi spectrometer employing the monochromatized Al Kα radiation. The photoluminescence (PL) spectra were measured on a Varian Cary Eclipse fluorescence spectrophotometer using the excitation light of 365 nm.

2.9 Photocatalytic H$_2$ evolution reactions

The photocatalytic H$_2$ evolution activities were tested on a Labsolar-6A online H$_2$ evolution and detection system (PerfectLight, Beijing Co., Ltd.). Specifically, 10 mg of photocatalyst was well dispersed into 100 mL aqueous lactic acid solution (20 vol.%) by sonication. Then, the obtained uniform suspension was filled into the reactor and vacuumized to remove the dissolved air. A 300-W Xe lamp (PLS-SXE300D) with a 420-nm cutoff filter was used as the light source. The test temperature was maintained at 10 °C controlled by a homothermic circulating pump. Lactic acid solution, TEOA (20 vol.%), ascorbic acid (0.375 M), and 0.35 M Na$_2$S/0.25 M Na$_2$SO$_3$ aqueous solution were respectively used as hole scavenger to study their influence on photocatalytic H$_2$ evolution activity. A 420-nm bandpass filter was used to determine the apparent quantum yield (AQY) of photocatalyst (10 mg) based on the following calculation equation

$$AQY = \frac{\text{Number of reacted electrons}}{\text{Number of incident photons}} \times 100\%$$
$$= \frac{2 \times \text{Number of evolved H}_2 \text{ molecules}}{\text{Number of incident photons}} \times 100\%$$

## 2.10 Electrochemical and photoelectrochemical measurements

The electrocatalytic HER measurements were carried out with a CHI 660E electrochemical station, where the reference electrode, counter electrode, and working electrode were Ag/AgCl, graphite rod, and glassy carbon electrode, respectively. To prepare the working electrode, 4 mg sample and 4 μL nafion were mixed with 0.8 mL water and 0.2 mL ethanol through sonication for 1 h to form a homogeneous ink. Then, 5 μL ink was loaded onto a polished glassy carbon electrode with an active area of 0.196 cm^2. Linear sweep voltammetry analyses were implemented in 0.5 M H$_2$SO$_4$ aqueous solution (purged with high-purity Ar gas) using the scanning rate of 10 mV·s^{-1}.

The Mott–Schottky curves, photocurrent and electrochemical impedance spectra (EIS) tests were performed on a standard three-electrode setup (CHI 660E). The photocatalyst-coated fluorine-doped tin oxide (FTO) electrode, Ag/AgCl, and Pt plate were used as the working electrode, reference electrode, and counter electrode, respectively. Among them, the working electrode was prepared according to our previous work [40]. The Mott–Schottky curves were tested in 0.5 M Na$_2$SO$_4$ aqueous solution. The amplitude and frequency were fixed at 0.01 V and 500 Hz, respectively. A 10 vol.% aqueous lactic acid solution was used as the electrolyte in the photocurrent response test with the applied sinusoidal voltage of 500 mV. In EIS test, 0.5 M Na$_2$SO$_4$ aqueous solution was selected as electrolyte with the amplitude of 0.005 V and frequency of 0.01–10^6 Hz, respectively.

3 Results and discussion

3.1 Catalyst characterization

The synthesis of CdS/Cd$_{0.5}$Zn$_{0.5}$S-Mo$_{1-x}$W$_x$S$_2$ hybrid hollow nano-spheres was carried out employing a template-assisted method followed by a self-assembling hybridization process. Here, the SiO$_2$ spheres served as sacrificial template for constructing novel nano-architectures with a hollow interior. As schematically depicted in Fig. 1, the fabrication of CdS/Cd$_{0.5}$Zn$_{0.5}$S-Mo$_{1-x}$W$_x$S$_2$ hybrid hollow nano-spheres can be divided into four steps. Firstly, CdS nanocrystals were coated onto the SiO$_2$ template to form SiO$_2$/CdS core–shell nano-spheres through the ultrasound-assisted water-bath reaction, as described in the experimental section. Second, by using the SiO$_2$/CdS nano-spheres as growth substrate, the SiO$_2$/CdS/
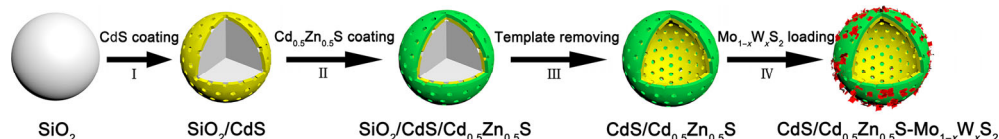
Figure 1 Schematic depicting the fabrication of CdS/Cd$_{0.5}$Zn$_{0.5}$S-Mo$_{1-x}$W$_x$S$_2$ hybrid hollow nano-spheres.

Cd$_{0.5}$Zn$_{0.5}$S nano-spheres were produced after the deposition of Cd$_{0.5}$Zn$_{0.5}$S nanocrystals by the similar procedure for CdS coating. During the growth of CdS or Cd$_{0.5}$Zn$_{0.5}$S shell, the citrate could react with Cd^{2+} or Cd^{2+}/Zn^{2+} ions at first to generate complexes [41], while the existence of ammonia caused the decomposition of thiourea into S^{2-} ions, which then combined with the free Cd^{2+} or Cd^{2+}/Zn^{2+} ions in solution to form CdS or Cd$_{0.5}$Zn$_{0.5}$S nanocrystals. Due to the formation of Cd–citrate and Cd/Zn–citrate complexes, the Cd^{2+} and Cd^{2+}/Zn^{2+} ions were released slowly, leading to the smooth deposition of CdS and Cd$_{0.5}$Zn$_{0.5}$S coating layers onto SiO$_2$ and SiO$_2$/CdS, respectively. In the third step, the CdS/Cd$_{0.5}$Zn$_{0.5}$S hollow nano-spheres were obtained when the SiO$_2$ core of SiO$_2$/CdS/Cd$_{0.5}$Zn$_{0.5}$S was removed via HF etching. Finally, the unique CdS/Cd$_{0.5}$Zn$_{0.5}$S-Mo$_{1-x}$W$_x$S$_2$ hybrid hollow nano-spheres can be fabricated by coupling the CdS/Cd$_{0.5}$Zn$_{0.5}$S with few-layered Mo$_{1-x}$W$_x$S$_2$ nanosheets through the self-assembly process under stirring condition.

The TEM photos in Figs. 2(a) and 2(e) display that, the SiO$_2$ template is composed of many uniform solid spheres with an average diameter of ~ 180 nm. After ultrasonic water-bath reaction at 65 °C for 70 min, the CdS-coated SiO$_2$ core–shell nano-spheres (SiO$_2$/CdS) were produced, which exhibit an increased particle-size (~ 190 nm) and rough surface as compared to the pristine SiO$_2$ template (Figs. 2(b) and 2(f)). Following the similar method for CdS coating, the SiO$_2$/CdS nano-spheres were coated by Cd$_{0.5}$Zn$_{0.5}$S nanocrystals to form the SiO$_2$/CdS/Cd$_{0.5}$Zn$_{0.5}$S ternary complex nano-spheres (Figs. 2(c) and 2(g)). Moreover, it can be seen from Fig. S1 in the Electronic Supplementary Material (ESM) that the diameter of SiO$_2$/CdS/Cd$_{0.5}$Zn$_{0.5}$S nano-spheres is raised with the prolonging

reaction duration. When the SiO$_2$ core of SiO$_2$/CdS/Cd$_{0.5}$Zn$_{0.5}$S nano-spheres (6 h Cd$_{0.5}$Zn$_{0.5}$S-coating) was removed via HF etching, the CdS/Cd$_{0.5}$Zn$_{0.5}$S hollow nano-spheres possessing a diameter of ~ 205 nm were obtained (Figs. 2(d) and 2(h)). According to the HRTEM analyses of the CdS/Cd$_{0.5}$Zn$_{0.5}$S shell in Fig. 2(i), the 0.334-nm lattice spacing matches well with (111) plane of CdS, while the outer fringes of 0.330 nm are recognized as (111) plane of Cd$_{0.5}$Zn$_{0.5}$S (CZ$_{0.5}$S). Furthermore, the STEM image and corresponding EDX elementary mapping results of CdS/Cd$_{0.5}$Zn$_{0.5}$S (Fig. 2(j)) corroborate the distribution of Cd, Zn, and S elements in the shell part of hollow nano-sphere. The elementary compositions of CdS/Cd$_{0.5}$Zn$_{0.5}$S were further measured by EDX and the results are displayed in Fig. S2(a) and Table S1 in the ESM. What's more, the well-defined spherical architecture of CdS/Cd$_{0.5}$Zn$_{0.5}$S is further confirmed by the SEM observation in Fig. 2(k). In addition, Fig. 2(l) indicates the major diameter of CdS/Cd$_{0.5}$Zn$_{0.5}$S hollow nano-spheres is around 200 nm, in agreement with the TEM result. On the other hand, the TEM images in Fig. S3 in the ESM reveal that both the Cd$_{0.5}$Zn$_{0.5}$S solid nano-spheres and CdS hollow nano-spheres are endowed with regular morphology and uniform size-distribution.

The TEM image in Fig. 3(a) indicates that the Mo$_{0.5}$W$_{0.5}$S$_2$ consists of many well-defined nanosheets. Moreover, the microstructure of Mo$_{0.5}$W$_{0.5}$S$_2$ nanosheets was further studied by HRTEM test. As shown in Fig. 3(b), the Mo$_{0.5}$W$_{0.5}$S$_2$ nanosheets (MW$_{0.5}$S) exhibit the layered structure with a spacing of 0.952 nm ((002) plane), which indicates that the layer spacing of our Mo$_{0.5}$W$_{0.5}$S$_2$ nanosheets is amplified in comparison with that of bulk MoS$_2$ [33]. Additionally, the nanosheets consist of merely few layers, suggesting the ultrathin characteristic of Mo$_{0.5}$W$_{0.5}$S$_2$
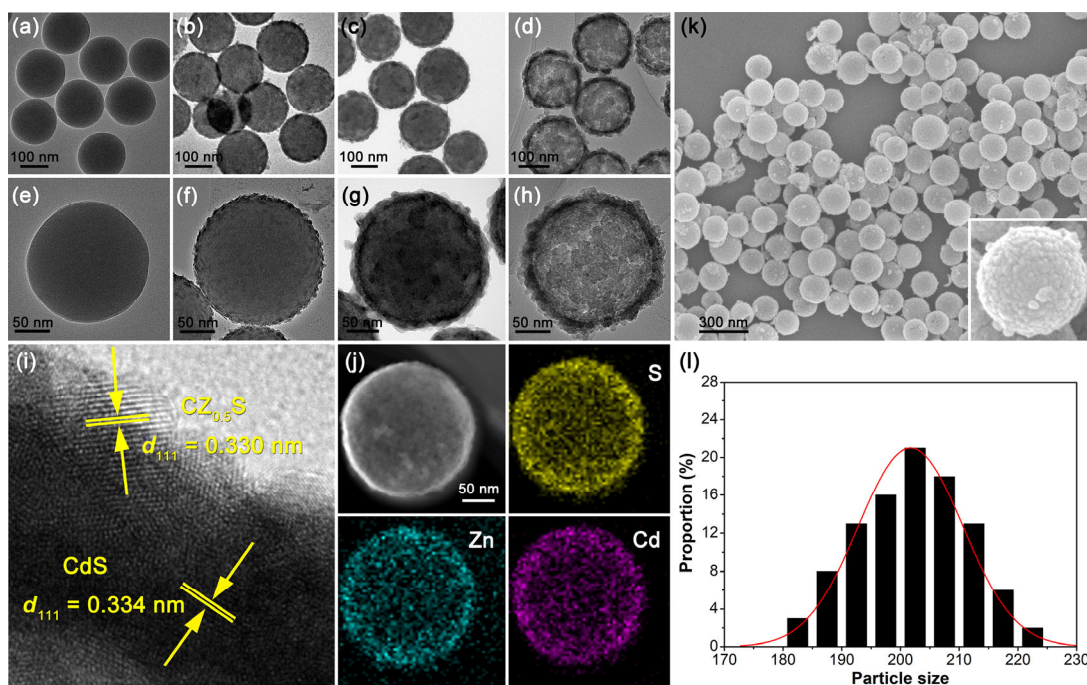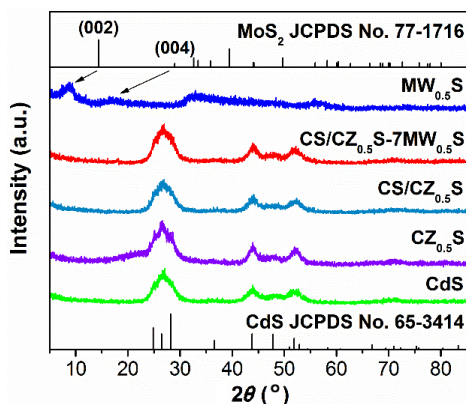

Figure 2 (a)–(h) TEM images of ((a) and (e)) SiO$_2$ solid spheres, ((b) and (f)) SiO$_2$/CdS solid nano-spheres, ((c) and (g)) SiO$_2$/CdS/Cd$_{0.5}$Zn$_{0.5}$S solid nano-spheres, and ((d) and (h)) CdS/Cd$_{0.5}$Zn$_{0.5}$S hollow nano-spheres. (i) HRTEM image and (j) STEM and corresponding EDX mapping results of CdS/Cd$_{0.5}$Zn$_{0.5}$S hollow nano-spheres. (k) SEM graph and (l) corresponding size-distribution histogram of CdS/Cd$_{0.5}$Zn$_{0.5}$S hollow nano-spheres.
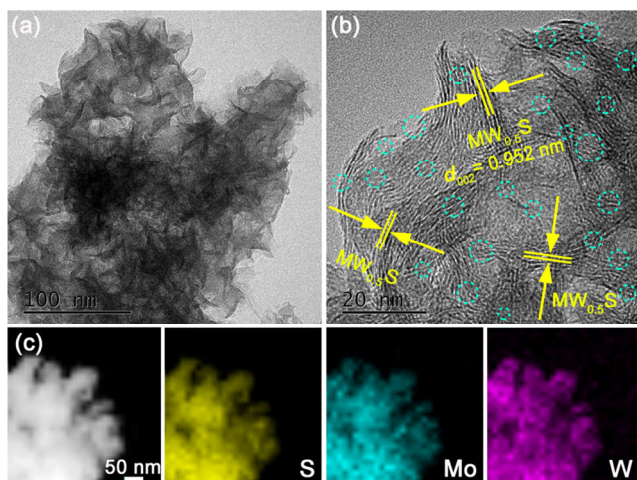
Figure 3 (a) TEM, (b) HRTEM, together with (c) STEM and EDX elementary mapping results of the $Mo_{0.5}W_{0.5}S_2$ nanosheets.

nanosheets. Noticeably, a large number of structural defects, such as lattice distortion and missing (highlighted in cyan dashed circles) exist in the $Mo_{0.5}W_{0.5}S_2$ nanosheets. What's more, $Mo_{0.5}W_{0.5}S_2$ nanosheets display the intense EPR signal around 2.006 (Fig. S4 in the ESM), which verifies the presence of S vacancies [42, 43]. These defect-rich $Mo_{0.5}W_{0.5}S_2$ ultrathin nanosheets could provide abundant active sites to facilitate the photocatalytic reaction efficiently [37]. Besides, the homogeneous distribution of S, Mo, and W elements in the $Mo_{0.5}W_{0.5}S_2$ nanosheets is manifested by the STEM and corresponding EDX mapping graphs in Fig. 3(c).

The crystalline phase of synthesized samples was investigated by XRD measurements. As disclosed in Fig. 4, both CdS hollow nano-spheres and $Cd_{0.5}Zn_{0.5}S$ solid nano-spheres ($CZ_{0.5}S$) show the diffraction signals assigned to wurtzite CdS (JCPDS No. 65-3414). The broadened XRD peaks of CdS hollow nano-spheres and $Cd_{0.5}Zn_{0.5}S$ solid nano-spheres indicate that they could be produced by the assembly of smaller nano-crystals. After the CdS hollow nano-spheres were coated by $Cd_{0.5}Zn_{0.5}S$ layer via ultrasonic water-bath reaction, the obtained $CdS/Cd_{0.5}Zn_{0.5}S$ hybrid hollow nano-spheres with different shell thicknesses exhibit the diffraction spectrum similar to that of individual CdS and $Cd_{0.5}Zn_{0.5}S$ (Fig. S5 in the ESM). It can be noticed that, $Mo_{0.5}W_{0.5}S_2$ nanosheets ($MW_{0.5}S$) possess the lowered angles of (002) and (004) diffractions compared to standard card (JCPDS No. 77-1716), which suggests that the layer spacing of our $Mo_{0.5}W_{0.5}S_2$ nanosheets was enlarged [33]. Moreover, Fig. S6(a) in the ESM also displays the low-angle-shifting of (002) and (004) peaks of MoS_2 and WS_2 nanosheets

in relation to the bulk counterparts, revealing the expanded layer structure of prepared MoS_2 and WS_2 nanosheets. The Raman signals of $Mo_{0.5}W_{0.5}S_2$ nanosheets are different from that of MoS_2 and WS_2 nanosheets (Fig. S6(b) in the ESM), which implies that the $Mo_{0.5}W_{0.5}S_2$ nanosheets are solid solutions rather than the mixture of MoS_2 and WS_2 nanosheets [44]. The increased layer spacing of $Mo_{0.5}W_{0.5}S_2$ nanosheets could facilitate their exfoliation into ultrathin nanosheets with abundant catalytic active sites. In addition, the $CS/CZ_{0.5}S$-7$MW_{0.5}S$ hybrid hollow nano-spheres present the diffraction peaks belonging to $CdS/Cd_{0.5}Zn_{0.5}S$ component, but the signals for $Mo_{0.5}W_{0.5}S_2$ component are not found because of the lower content and crystallinity of the loaded $Mo_{0.5}W_{0.5}S_2$ nanosheets.

Optical property of the samples was studied by UV–vis diffuse reflectance spectroscopy. It is seen from Fig. 5 that, the $Cd_{0.5}Zn_{0.5}S$ solid nano-spheres ($CZ_{0.5}S$) are in possession of a good response to visible light. The absorption edge of $Cd_{0.5}Zn_{0.5}S$ solid nano-spheres is around 504.7 nm, which is red-shifted to 546.5 nm when the CdS hollow nano-spheres are concerned. After the CdS hollow nano-spheres were coated by $Cd_{0.5}Zn_{0.5}S$ layer, the resultant $CdS/Cd_{0.5}Zn_{0.5}S$ hybrid hollow nano-spheres ($CS/CZ_{0.5}S$) were provided with an enhanced light-absorption capability and the corresponding absorption edge is identified as 551.8 nm. Interestingly, the $Mo_{0.5}W_{0.5}S_2$ nanosheets ($MW_{0.5}S$) exhibit a quite strong absorption throughout the whole visible-light region. As a result, the $CS/CZ_{0.5}S$-7$MW_{0.5}S$ hybrid hollow nano-spheres display a dramatically improved capacity for light-harvest, which contributes to the generation of more available charges to promote the photocatalytic reaction significantly. Moreover, compared with the $CS/CZ_{0.5}S$-7MS and $CS/CZ_{0.5}S$-7WS counterparts, the $CS/CZ_{0.5}S$-7$MW_{0.5}S$ exhibits intensified light-absorption in the region beyond 550 nm, suggesting that the photocatalytic efficiency could be effectively heightened by the latter under visible-light irradiation.

The composition and microstructure of $CS/CZ_{0.5}S$-7$MW_{0.5}S$ composite were inspected by TEM measurement. As depicted in Fig. 1, the $CS/CZ_{0.5}S$-7$MW_{0.5}S$ was prepared after the ultrasonically-exfoliated $Mo_{0.5}W_{0.5}S_2$ nanosheets were loaded onto $CdS/Cd_{0.5}Zn_{0.5}S$ hollow nano-spheres through the self-assembly process under stirring condition. The TEM photo in Fig. 6(a) exhibits that, the $CS/CZ_{0.5}S$-7$MW_{0.5}S$ composite is in possession of a hollow spherical architecture similar to that of $CdS/Cd_{0.5}Zn_{0.5}S$. Moreover, the lattice structure of $CS/CZ_{0.5}S$-7$MW_{0.5}S$ was further investigated by HRTEM analyses. According to Fig. 6(b), the few-layered nanosheets coating on the outer surface of hybrid are recognized as $Mo_{0.5}W_{0.5}S_2$ ($MW_{0.5}S$), in which an expanded layer spacing of 0.952 nm ((002) plane) can be observed. In addition, the fringes having

Figure 4 XRD patterns of CdS, $Cd_{0.5}Zn_{0.5}S$, $CdS/Cd_{0.5}Zn_{0.5}S$, $Mo_{0.5}W_{0.5}S_2$, and $CS/CZ_{0.5}S$-7$MW_{0.5}S$.
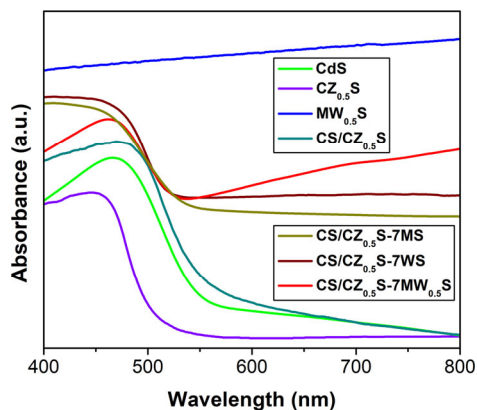
Figure 5 UV–vis absorption spectra of CdS, $Cd_{0.5}Zn_{0.5}S$, $CdS/Cd_{0.5}Zn_{0.5}S$, $Mo_{0.5}W_{0.5}S_2$, $CS/CZ_{0.5}S$-7MS, $CS/CZ_{0.5}S$-7WS, and $CS/CZ_{0.5}S$-7$MW_{0.5}S$.
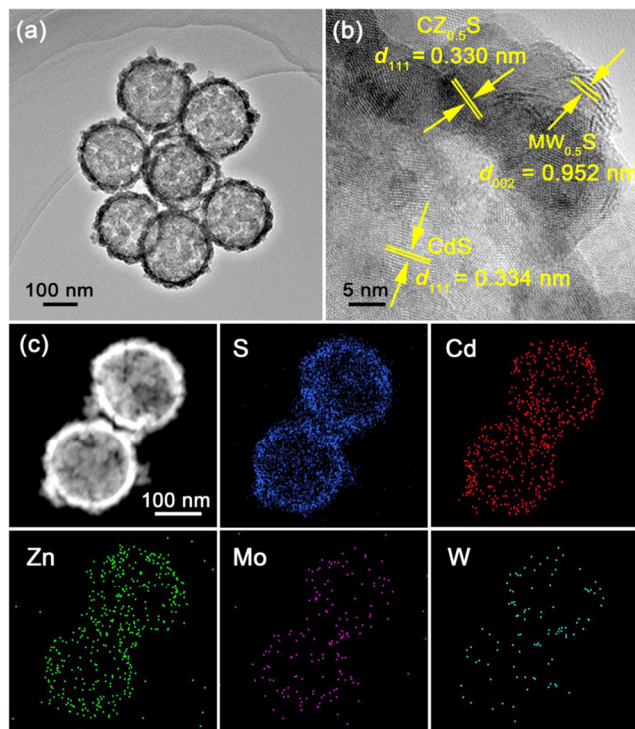
Figure 6 (a) TEM, (b) HRTEM, as well as (c) STEM and corresponding EDX elementary mapping photos of the CS/CZ$_{0.5}$S-7MW$_{0.5}$S hybrid hollow nano-spheres.

0.330-nm spacing are associated with (111) plane of Cd$_{0.5}$Zn$_{0.5}$S (CZ$_{0.5}$S), while the 0.334-nm lattices are attributed to the (111) plane of CdS. Furthermore, the STEM and corresponding EDX elementary mapping images of CS/CZ$_{0.5}$S-7MW$_{0.5}$S are displayed in Fig. 6(c), which evince the elementary distribution of S, Cd, Zn, Mo, and W throughout the whole nano-sphere. The elementary compositions of CS/CZ$_{0.5}$S-7MW$_{0.5}$S were

analyzed by EDX test and the results are given in Fig. S2(b) and Table S1 in the ESM. Therefore, the composition and structure of CS/CZ$_{0.5}$S-7MW$_{0.5}$S hybrid hollow nano-spheres are well confirmed by the above TEM, HRTEM, EDX, as well as STEM and EDX elementary mapping results.

XPS spectra were measured to obtain the information about the surface composition and valence states of the samples. For explication, the XPS spectra of CS/CZ$_{0.5}$S-10MW$_{0.5}$S hybrid are illustrated in Fig. 7, where the data of CdS/Cd$_{0.5}$Zn$_{0.5}$S (CS/CZ$_{0.5}$S) and Mo$_{0.5}$W$_{0.5}$S$_2$ (MW$_{0.5}$S) are also given for reference. The Cd 3d and Zn 2p doublet peaks of CdS/Cd$_{0.5}$Zn$_{0.5}$S are observed at 405.3–412.1 and 1,021.9–1,045.1 eV (Figs. 7(a) and 7(b)), which can be assigned to the Cd^{2+} and Zn^{2+} ions [23, 45], respectively. In comparison with CdS/Cd$_{0.5}$Zn$_{0.5}$S, the Cd 3d and Zn 2p signals of CS/CZ$_{0.5}$S-10MW$_{0.5}$S are moved toward higher binding energies. As shown in Fig. 7(c), two sets of doublet signals at 228.9–232.1 and 229.7–232.9 eV are discerned from the Mo 3d spectrum of Mo$_{0.5}$W$_{0.5}$S$_2$, indicating the existence of Mo^{4+} and Mo^{5+} species [46, 47]. Meanwhile, the doublet peaks locating at 232.7–235.9 eV could be associated with the Mo^{6+} ions formed due to surface oxidation [48]. Based on Fig. 7(d), the W 4f spectrum of Mo$_{0.5}$W$_{0.5}$S$_2$ consists of two sets of doublet peaks at 32.6–34.7 and 36.0–38.1 eV, which correspond to the W^{4+} and W^{6+} valence states [39, 49], respectively. Compared with Mo$_{0.5}$W$_{0.5}$S$_2$, the Mo and W signals of CS/CZ$_{0.5}$S-10MW$_{0.5}$S are shifted to lower binding energies. Therefore, the above results suggest the reduced Cd and Zn electron densities of CdS/Cd$_{0.5}$Zn$_{0.5}$S when it was coupled by Mo$_{0.5}$W$_{0.5}$S$_2$ to produce the CdS/Cd$_{0.5}$Zn$_{0.5}$S-Mo$_{0.5}$W$_{0.5}$S$_2$ hybrid, and oppositely, the Mo and W electron densities are increased after the hybridization reaction. The variation of electron cloud density originates from the electron transfer between the CdS/Cd$_{0.5}$Zn$_{0.5}$S and Mo$_{0.5}$W$_{0.5}$S$_2$ components of CdS/Cd$_{0.5}$Zn$_{0.5}$S-Mo$_{0.5}$W$_{0.5}$S$_2$, thus certifying the formation of intimate heterointerfaces in the composite [50]. In addition, the O 1s spectrum of Mo$_{0.5}$W$_{0.5}$S$_2$ can be fitted into three peaks at 530.3,
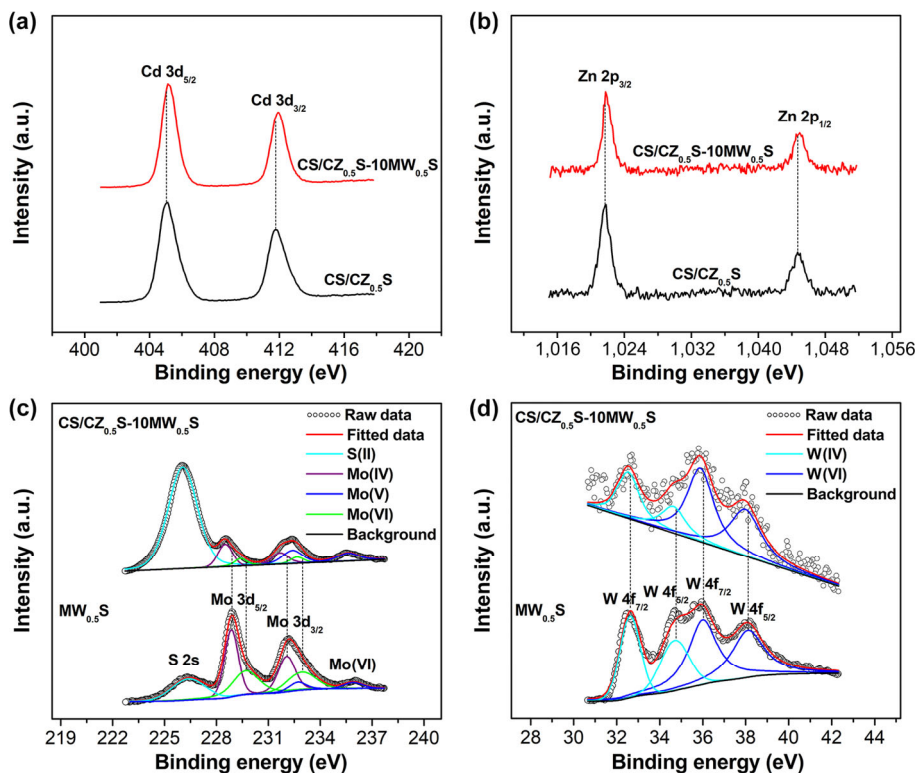

Figure 7 (a) Cd 3d and (b) Zn 2p XPS spectra of CdS/Cd$_{0.5}$Zn$_{0.5}$S and CS/CZ$_{0.5}$S-10MW$_{0.5}$S. (c) Mo 3d and (d) W 4f XPS spectra of Mo$_{0.5}$W$_{0.5}$S$_2$ and CS/CZ$_{0.5}$S-10MW$_{0.5}$S.

531.4, and 533.1 eV (Fig. S7(a) in the ESM), which are in accordance with that of Mo$^{(IV)}$-O species [33], −OH groups [51], and adsorbed H$_2$O [52], respectively. What's more, there are two sets of doublet signals (161.9–163.1 and 163.5–164.5 eV) present in the S 2p spectrum of Mo$_{0.5}$W$_{0.5}$S$_2$ (Fig. S7(b) in the ESM), verifying the generation of S$^{2−}$ and S$_2^{2−}$ species [53, 54]. Furthermore, the O 1s and S 2p signals of CS/CZ$_{0.5}$S-10MW$_{0.5}$S are similar to that of Mo$_{0.5}$W$_{0.5}$S$_2$, which confirms that the O and S species of Mo$_{0.5}$W$_{0.5}$S$_2$ are preserved in CdS/Cd$_{0.5}$Zn$_{0.5}$S-Mo$_{0.5}$W$_{0.5}$S$_2$ composite. Previous studies have demonstrated that both the Mo^{5+} and S$_2^{2−}$ can serve as the active sites for H$_2$ evolution [47, 55, 56]. Thus, the CdS/Cd$_{0.5}$Zn$_{0.5}$S-Mo$_{0.5}$W$_{0.5}$S$_2$ hybrids with these Mo^{5+} and S$_2^{2−}$ active species are anticipated to display an outstanding capability toward photocatalytic H$_2$ production.

3.2 Photocatalytic activity

The photocatalytic H$_2$ evolution activities of as-prepared samples were compared under visible-light irradiation. Figure S8 in the ESM reveals that the Cd$_{0.5}$Zn$_{0.5}$S solid nano-spheres (CZ$_{0.5}$S) have a higher HER activity than that of CdS solid and hollow nano-spheres. Compared with CdS hollow nano-spheres and Cd$_{0.5}$Zn$_{0.5}$S solid nano-spheres, the photocatalytic activity of CdS/Cd$_{0.5}$Zn$_{0.5}$S hybrid hollow nano-spheres is improved

and the CdS/Cd$_{0.5}$Zn$_{0.5}$S prepared after Cd$_{0.5}$Zn$_{0.5}$S-coating for 6 h (CS/CZ$_{0.5}$S) exhibits the best activity of 1.65 mmol·g^{-1}·h^{-1}. The enhanced HER activity of CdS/Cd$_{0.5}$Zn$_{0.5}$S than CdS could be ascribed to the formation of interfacial heterojunction which facilitates the transfer and separation of electron–hole pairs notably. However, Fig. 5 displays that the absorption edge of Cd$_{0.5}$Zn$_{0.5}$S is apparently blue-shifted as compared with that of CdS. Thus, the light-absorption of CdS/Cd$_{0.5}$Zn$_{0.5}$S composite will be weakened when the Cd$_{0.5}$Zn$_{0.5}$S content was raised to a higher value. Moreover, an excessive Cd$_{0.5}$Zn$_{0.5}$S loading could cause the unfavorable recombination of charge carriers. Consequently, the H$_2$ generation capability of CdS/Cd$_{0.5}$Zn$_{0.5}$S was decreased at a higher Cd$_{0.5}$Zn$_{0.5}$S amount due to the above reasons. Noticeably, when CdS/Cd$_{0.5}$Zn$_{0.5}$S was decorated by MoS$_2$ to form the CdS/Cd$_{0.5}$Zn$_{0.5}$S-MoS$_2$ hollow nano-spheres, the HER property is dramatically enhanced and the optimal activity of 131.25 mmol·g^{-1}·h^{-1} is attained at the 7 wt.%-MoS$_2$ content (CS/CZ$_{0.5}$S-7MS) (Fig. 8(a)). With the raise of MoS$_2$ content, the HER activity of CdS/Cd$_{0.5}$Zn$_{0.5}$S-MoS$_2$ is gradually improved due to the enhanced charge separation and increased active sites for H$_2$ evolution. However, an excess loading of MoS$_2$ could screen the light-absorption needed by CdS/Cd$_{0.5}$Zn$_{0.5}$S to drive the H$_2$ generation reaction, which leads to the lowered HER capability. Therefore, there exists an
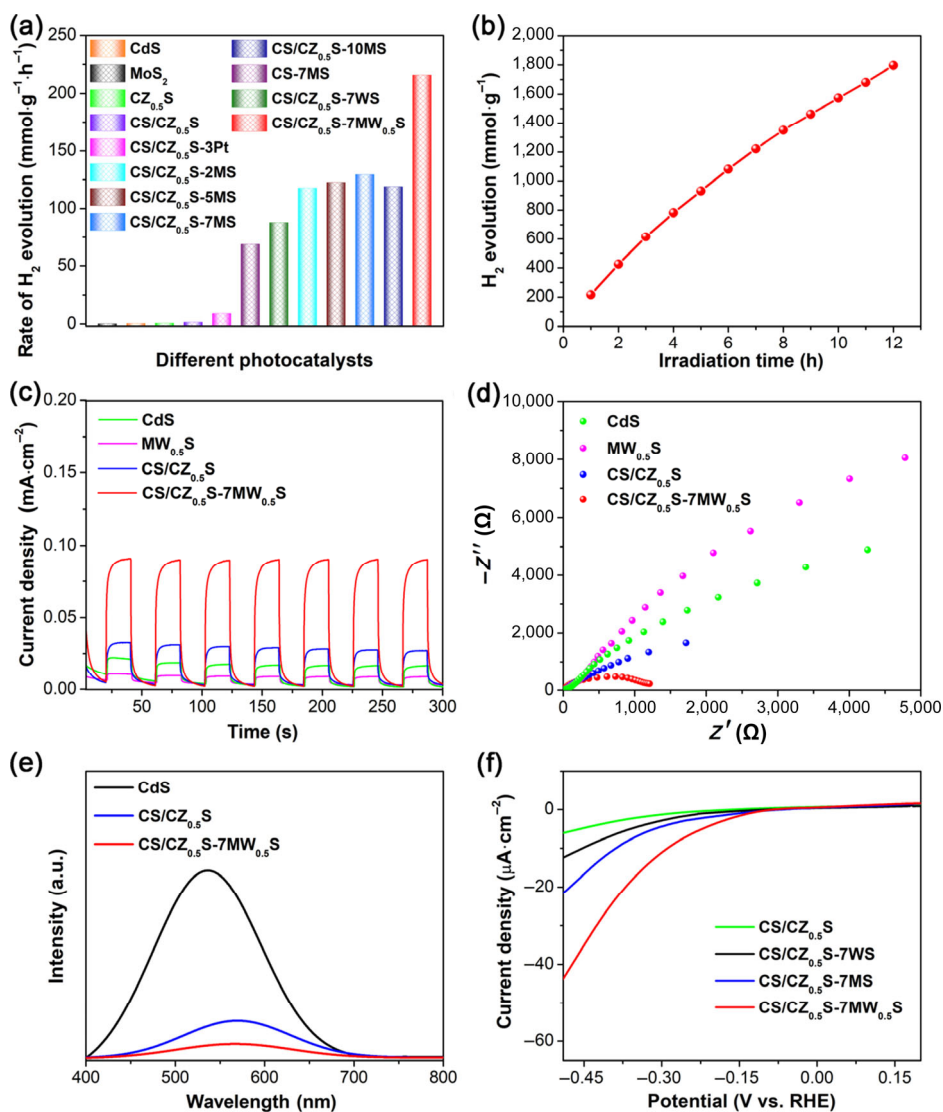
Figure 8 (a) Photocatalytic HER activities of different samples. (b) Steady H$_2$ evolution of CS/CZ$_{0.5}$S-7MW$_{0.5}$S for 12 h. (c) Transient photocurrent responses, (d) EIS spectra, and (e) PL emissions of CdS, CdS/Cd$_{0.5}$Zn$_{0.5}$S, Mo$_{0.5}$W$_{0.5}$S$_2$, and CS/CZ$_{0.5}$S-7MW$_{0.5}$S. (f) Polarization curves of the CdS/Cd$_{0.5}$Zn$_{0.5}$S, CS/CZ$_{0.5}$S-7WS, CS/CZ$_{0.5}$S-7MS, and CS/CZ$_{0.5}$S-7MW$_{0.5}$S electrodes.

optimal MoS_2 loading amount for the $CdS/Cd_{0.5}Zn_{0.5}S$-MoS_2 to achieve the maximum HER activity. The HER activity of $CS/CZ_{0.5}S$-7MS is much better than that of 3 wt.% Pt-loaded $CdS/Cd_{0.5}Zn_{0.5}S$ ($CS/CZ_{0.5}S$-3Pt) and the CdS-MoS_2 with the same MoS_2 content (CS-7MS). Interestingly, under the same loading concentration of 7 wt.%, the $Mo_{1-x}W_xS_2$-supported $CdS/Cd_{0.5}Zn_{0.5}S$ hollow nano-spheres ($CS/CZ_{0.5}S$-7MW$_x$S) display a much superior HER performance with respect to that of the MoS_2- and WS_2-coupled counterparts ($CS/CZ_{0.5}S$-7MS and $CS/CZ_{0.5}S$-7WS, Fig. S9 in the ESM). Moreover, the influence of W/Mo ratio on the HER activity of $CS/CZ_{0.5}S$-7MW$_x$S composites was investigated. It is seen that the $CS/CZ_{0.5}S$-7MW$_{0.5}$S with the W/Mo ratio of 1:1 presents the maximum H_2 generation rate of 215.99 mmol·g^{-1}·h^{-1}, approximately 24 and 131 times that of $CS/CZ_{0.5}S$-3Pt and $CdS/Cd_{0.5}Zn_{0.5}S$ hollow nano-spheres, respectively. The AQY of $CS/CZ_{0.5}S$-7MW$_{0.5}$S for H_2 evolution under 420-nm irradiation is as high as 64.81% (Fig. S10 in the ESM). We can see from Table S3 that, the HER activity of our $CS/CZ_{0.5}S$-7MW$_{0.5}$S hollow nano-spheres exceeds that of the great majority of reported photocatalysts containing CdS ingredient. Besides, the H_2 evolution activity of $CS/CZ_{0.5}S$-7MW$_{0.5}$S in different sacrificial agents was examined. As revealed by Fig. S11 in the ESM, the $CS/CZ_{0.5}S$-7MW$_{0.5}$S is much more reactive for H_2 formation in lactic acid solution than in Na_2S/Na_2SO_3, TEOA, and ascorbic acid solutions. The pH value of lactic acid solution (1.3) is lower than that of ascorbic acid (2.5), TEOA (10.8), and Na_2S/Na_2SO_3 (13.4) solutions. Therefore, there are more H^+ ions available for HER in lactic acid solution, which is responsible for the higher HER activity of $CS/CZ_{0.5}S$-7MW$_{0.5}$S in lactic acid solution than in the other three solutions. In addition, the $CS/CZ_{0.5}S$-7MW$_{0.5}$S hollow nano-spheres are also durable for cycling and long-term H_2 production under visible-light irradiation (Fig. 8(b) and Fig. S12 in the ESM), suggesting the huge prospect of $CS/CZ_{0.5}S$-7MW$_{0.5}$S for sustainable H_2 generation from solar-driven water-splitting.

The outstanding photocatalytic property of $CS/CZ_{0.5}S$-7MW$_{0.5}$S hollow nano-spheres can be associated with their distinguished charge separation efficiency. It is seen from Fig. 8(c) that, the photocurrent density of $CS/CZ_{0.5}S$-7MW$_{0.5}$S is much higher than that of $CdS/Cd_{0.5}Zn_{0.5}S$ ($CS/CZ_{0.5}S$), CdS, and $Mo_{0.5}W_{0.5}S_2$ (MW$_{0.5}$S), indicating the effectively depressed charge recombination by $CS/CZ_{0.5}S$-7MW$_{0.5}$S as compared with the latter three [57]. Moreover, the EIS Nyquist curves in Fig. 8(d) disclose that the arc diameter of $CS/CZ_{0.5}S$-7MW$_{0.5}$S is reduced in relation to that of $CdS/Cd_{0.5}Zn_{0.5}S$, CdS, and $Mo_{0.5}W_{0.5}S_2$, which signifies the $CS/CZ_{0.5}S$-7MW$_{0.5}$S has a smaller charge-transfer resistance than the other ones [58, 59], originating from the promoted separation and transmission of photogenerated charges in the former. In addition to photocurrent response and EIS data, PL measurement was further performed to study the charge separation efficiency of photocatalysts. Figure 8(e)

displays the PL signals of CdS, $CdS/Cd_{0.5}Zn_{0.5}S$, and $CS/CZ_{0.5}S$-7MW$_{0.5}$S. Evidently, the PL emission of $CS/CZ_{0.5}S$-7MW$_{0.5}$S is notably quenched by comparison to that of CdS and $CdS/Cd_{0.5}Zn_{0.5}S$, manifesting that the $CS/CZ_{0.5}S$-7MW$_{0.5}$S performs better in the suppression of charge recombination with respect to CdS and $CdS/Cd_{0.5}Zn_{0.5}S$ [60–62], which agrees well with the photocurrent and PL results. What's more, the $CS/CZ_{0.5}S$-7MW$_{0.5}$S shows prolonged PL lifetime than that of $CdS/Cd_{0.5}Zn_{0.5}S$ (Fig. S13 and Table S2 in the ESM), which confirms that the charge recombination of $CdS/Cd_{0.5}Zn_{0.5}S$ can be effectively hindered through the integration of $Mo_{0.5}W_{0.5}S_2$, resulting in a notably elongated lifetime of charge carriers [63, 64]. As is known to all, besides charge separation, the active sites of photocatalyst constitute another critical factor that can significantly facilitate the redox reactions occurring on the surface [19]. According to the polarization curves in Fig. 8(f), the electrocatalytic HER activity of $CdS/Cd_{0.5}Zn_{0.5}S$ is dramatically increased after the loading of WS_2, MoS_2, and $Mo_{0.5}W_{0.5}S_2$ cocatalysts. Furthermore, the $CS/CZ_{0.5}S$-7MW$_{0.5}$S exhibits a much superior HER activity in contrast with that of $CS/CZ_{0.5}S$-7WS and $CS/CZ_{0.5}S$-7MS, which matches well with the extraordinary photocatalytic H_2 evolution activity of $CS/CZ_{0.5}S$-7MW$_{0.5}$S composite. The abundant active sites existing in the defect-rich $Mo_{0.5}W_{0.5}S_2$ nanosheets are responsible for their outstanding cocatalytic activity toward H_2 production. In addition, the UV–vis absorption spectra in Fig. 5 indicate that the $CS/CZ_{0.5}S$-7MW$_{0.5}$S has much stronger light-absorption in the region beyond 550 nm than $CS/CZ_{0.5}S$-7WS and $CS/CZ_{0.5}S$-7MS, which contributes to the enhanced activity of the former toward photocatalytic H_2 production.

3.3 Photocatalytic mechanism

To probe into the origin for the prominent charge separation capability of $CdS/Cd_{0.5}Zn_{0.5}S$-$Mo_{0.5}W_{0.5}S_2$ composite, the electronic band structures of $Mo_{0.5}W_{0.5}S_2$ (MW$_{0.5}$S) and $CdS/Cd_{0.5}Zn_{0.5}S$ ($CS/CZ_{0.5}S$) were studied. According to Fig. 9(a), the flat-band potential is found from the Mott–Schottky plots to be −0.11 and −0.48 V vs. RHE for $Mo_{0.5}W_{0.5}S_2$ and $CdS/Cd_{0.5}Zn_{0.5}S$ respectively. Moreover, the positive slopes of Mott–Schottky curves indicate that both the $Mo_{0.5}W_{0.5}S_2$ and $CdS/Cd_{0.5}Zn_{0.5}S$ belonged to n-type semiconductor [65]. As we know, the conduction band (CB) bottom potential of an n-type semiconductor is moved upward by 0.1 V with respect to its flat band potential [66]. Hence, the conduction band bottom potential of $Mo_{0.5}W_{0.5}S_2$ and $CdS/Cd_{0.5}Zn_{0.5}S$ is fixed as −0.21 and −0.58 V vs. RHE, respectively. Ordinarily, the bandgap energies of semiconductors can be estimated by the Kubelka–Munk formula: $(Ah\nu)^n = K(h\nu - E_g)$ [67, 68], where A stands for the absorbance, $h\nu$ denotes the photon energy, K represents a constant, E_g is the bandgap, and n takes 0.5 or 2 for indirect-transition or direct-transition semiconductors, respectively. Figure S14 in the ESM displays that the bandgap of $Mo_{0.5}W_{0.5}S_2$
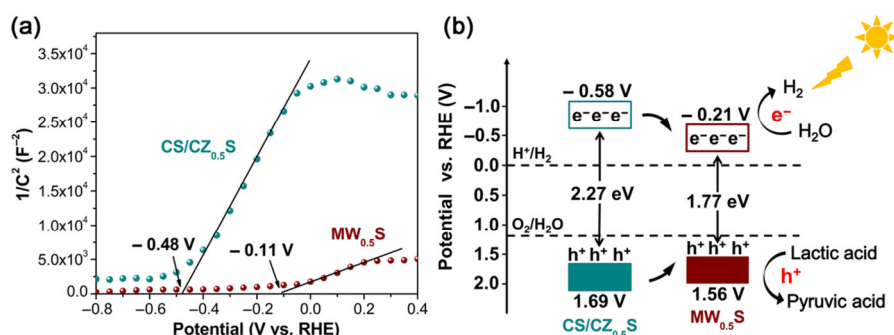
Figure 9 (a) Mott–Schottky curves and (b) band alignments of $Mo_{0.5}W_{0.5}S_2$ and $CdS/Cd_{0.5}Zn_{0.5}S$.

and CdS/Cd$_{0.5}$Zn$_{0.5}$S is 1.77 and 2.27 eV, respectively. Based on the bandgaps of Mo$_{0.5}$W$_{0.5}$S$_2$ and CdS/Cd$_{0.5}$Zn$_{0.5}$S and their conduction band bottom positions, the corresponding band alignments could be established. We can see from Fig. 9(b) that the CB minimum level of CdS/Cd$_{0.5}$Zn$_{0.5}$S is higher than that of Mo$_{0.5}$W$_{0.5}$S$_2$, while the valence band (VB) maximum level of CdS/Cd$_{0.5}$Zn$_{0.5}$S is lowered as compared with that of Mo$_{0.5}$W$_{0.5}$S$_2$. Therefore, under visible-light irradiation, the photogenerated electrons will transfer from the CdS/Cd$_{0.5}$Zn$_{0.5}$S CB to the Mo$_{0.5}$W$_{0.5}$S$_2$ CB; in contrast, the photo-holes left in the CdS/Cd$_{0.5}$Zn$_{0.5}$S VB could spontaneously migrate to the Mo$_{0.5}$W$_{0.5}$S$_2$ VB as a result of the existed potential difference. Subsequently, these photo-induced electrons and holes would participate in the reduction and oxidation reactions, respectively, leading to an effective separation of charge carriers. In addition, there exists substantial amount of HER active sites in the defect-rich Mo$_{0.5}$W$_{0.5}$S$_2$ ultrathin nanosheets (Figs. 3 and 7). What's more, the CdS/Cd$_{0.5}$Zn$_{0.5}$S hollow structure helps to promote the scattering and absorption of incident light and shorten the charge transport and separation distance as well [19]. Benefiting from the above advantages, the CdS/Cd$_{0.5}$Zn$_{0.5}$S-Mo$_{0.5}$W$_{0.5}$S$_2$ hybrid hollow nano-spheres are endowed with an outstanding performance toward photocatalytic H$_2$ evolution from water-splitting.

4   Conclusions

In conclusion, a unique photocatalyst comprising CdS/Cd$_{0.5}$Zn$_{0.5}$S hollow nano-spheres decorated with defect-rich Mo$_{1-x}$W$_x$S$_2$ ultrathin nanosheets (CdS/Cd$_{0.5}$Zn$_{0.5}$S-Mo$_{1-x}$W$_x$S$_2$) was synthesized for the first time. Compared with CdS, CdS/Cd$_{0.5}$Zn$_{0.5}$S, and Pt-loaded CdS/Cd$_{0.5}$Zn$_{0.5}$S, the optimized CdS/Cd$_{0.5}$Zn$_{0.5}$S-Mo$_{1-x}$W$_x$S$_2$ hybrid hollow nano-spheres exhibit a highly promoted visible-light-induced H$_2$ production rate of 215.99 mmol·g^{-1}·h^{-1} (AQY of 64.81% at 420 nm), outperforming that of most reported CdS-based photocatalysts. Such a dramatic enhancement on the photocatalytic capability can be attributed to the CdS/Cd$_{0.5}$Zn$_{0.5}$S-Mo$_{1-x}$W$_x$S$_2$ hollow nanostructure that brings about excellent light harvesting, the presence of abundant active sites in the defective Mo$_{1-x}$W$_x$S$_2$ cocatalyst, as well as the facilitated charge isolation and transportation through the interfacial heterojunctions. In addition, the CdS/Cd$_{0.5}$Zn$_{0.5}$S-Mo$_{1-x}$W$_x$S$_2$ composites are also provided with favourable cycling and long-term stability for H$_2$ production under light irradiation. Our work can shed light on the designed synthesis of novel hollow nanostructures toward efficient photocatalytic reactions.

Electronic Supplementary Material: Supplementary material (bandgaps, EPR signal, EDX spectra, Raman spectra, time-resolved PL spectra, tables summarizing the elementary compositions, fitted PL lifetimes, and reported HER data, as well as additional XRD patterns, XPS spectra, TEM images, and HER activities) is available in the online version of this article at https://doi.org/10.1007/s12274-021-3585-7.

References

[1]   Zhang, J.; Wang, T.; Liu, P.; Liao, Z. Q.; Liu, S. H.; Zhuang, X. D.; Chen, M. W.; Zschech, E.; Feng, X. L. Efficient hydrogen production on MoNi$_4$ electrocatalysts with fast water dissociation kinetics. *Nat. Commun.* **2017**, *8*, 15437.

[2]   Wang, Z.; Li, C.; Domen, K. Recent developments in heterogeneous photocatalysts for solar-driven overall water splitting. *Chem. Soc. Rev.* **2019**, *48*, 2109–2125.

[3]   Low, J.; Yu, J. G.; Jaroniec, M.; Wageh, S.; Al-Ghamdi, A. A. Heterojunction photocatalysts. *Adv. Mater.* **2017**, *29*, 1601694.

[4]   Wang, H. L.; Zhang, L. S.; Chen, Z. G.; Hu, J. Q.; Li, S. J.; Wang, Z. H.; Liu, J. S.; Wang, X. C. Semiconductor heterojunction photocatalysts: Design, construction, and photocatalytic performances. *Chem. Soc. Rev.* **2014**, *43*, 5234–5244.

[5]   Tian, S. F.; Chen, S. D.; Ren, X. T.; Cao, R. H.; Hu, H. Y.; Bai, F. Bottom-up fabrication of graphitic carbon nitride nanosheets modified with porphyrin via covalent bonding for photocatalytic H$_2$ evolution. *Nano Res.* **2019**, *12*, 3109–3115.

[6]   Tan, X. N.; Zhang, J. L.; Tan, D. X.; Shi, J. B.; Cheng, X. Y.; Zhang, F. Y.; Liu, L. F.; Zhang, B. X.; Su, Z. Z.; Han, B. X. Ionic liquids produce heteroatom-doped Pt/TiO$_2$ nanocrystals for efficient photocatalytic hydrogen production. *Nano Res.* **2019**, *12*, 1967–1972.

[7]   Wei, Y. Z.; Wang, J. Y.; Yu, R. B.; Wan, J. W.; Wang, D. Constructing SrTiO$_3$-TiO$_2$ heterogeneous hollow multi-shelled structures for enhanced solar water splitting. *Angew. Chem., Int. Ed.* **2019**, *58*, 1422–1426.

[8]   Yuan, Y. J.; Chen, D. Q.; Yu, Z. T.; Zou, Z. G. Cadmium sulfide-based nanomaterials for photocatalytic hydrogen production. *J. Mater. Chem. A* **2018**, *6*, 11606–11630.

[9]   Chandrasekaran, S.; Yao, L.; Deng, L. B.; Bowen, C.; Zhang, Y.; Chen, S. M.; Lin, Z. Q.; Peng, F.; Zhang, P. X. Recent advances in metal sulfides: From controlled fabrication to electrocatalytic, photocatalytic and photoelectrochemical water splitting and beyond. *Chem. Soc. Rev.* **2019**, *48*, 4178–4280.

[10] Zhu, Y. X.; Jiang, X.; Lin, L.; Wang, S. H.; Chen, C. Fabrication of ZnS/CdS heterojunction by using bimetallic MOFs template for photocatalytic hydrogen generation. *Chem. Res. Chin. Univ.* **2020**, *36*, 1032–1038.

[11] Yu, Y.; Yan, W.; Wang, X. F.; Li, P.; Gao, W. Y.; Zou, H. H.; Wu, S. M.; Ding, K. J. Surface engineering for extremely enhanced charge separation and photocatalytic hydrogen evolution on g-C$_3$N$_4$. *Adv. Mater.* **2018**, *30*, 1705060.

[12] Ong, W. J.; Tan, L. L.; Ng, Y. H.; Yong, S. T.; Chai, S. P. Graphitic carbon nitride (g-C$_3$N$_4$)-based photocatalysts for artificial photosynthesis and environmental remediation: Are we a step closer to achieving sustainability? *Chem. Rev.* **2016**, *116*, 7159–7329.

[13] Sun, T.; Wang, C. X.; Xu, Y. X. Covalent triazine framework nanosheets for efficient energy storage and conversion. *Chem. Res. Chin. Univ.* **2020**, *36*, 640–647.

[14] Fujishima, A.; Honda, K. Electrochemical photolysis of water at a semiconductor electrode. *Nature* 1972, *238*, 37–38.

[15] Zhang, S. W.; Yang, H. C.; Gao, H. H.; Cao, R. Y.; Huang, J. Z.; Xu, X. J. One-pot synthesis of CdS irregular nanospheres hybridized with oxygen-incorporated defect-rich MoS$_2$ ultrathin nanosheets for efficient photocatalytic hydrogen evolution. *ACS Appl. Mater. Interfaces* 2017, *9*, 23635–23646.

[16] Cheng, L.; Xiang, Q. J.; Liao, Y. L.; Zhang, H. W. CdS-based photocatalysts. *Energy Environ. Sci.* **2018**, *11*, 1362–1391.

[17] Liu, M. C.; Jing, D. W.; Zhou, Z. H.; Guo, L. J. Twin-induced one-dimensional homojunctions yield high quantum efficiency for solar hydrogen generation. *Nat. Commun.* **2013**, *4*, 2278.

[18] Zhang, P.; Wang, S. B.; Guan, B. Y.; Lou, X. W. Fabrication of CdS hierarchical multi-cavity hollow particles for efficient visible light CO$_2$ reduction. *Energy Environ. Sci.* **2019**, *12*, 164–168.

[19] Xiao, M.; Wang, Z. L.; Lyu, M.; Luo, B.; Wang, S. C.; Liu, G.; Cheng, H. M.; Wang, L. Z. Hollow nanostructures for photocatalysis: Advantages and challenges. *Adv. Mater.* **2019**, *31*, 1801369.

[20] Wei, Y. Z.; Yang, N. L.; Huang, K. K.; Wan, J. W.; You, F. F.; Yu, R. B.; Feng, S. H.; Wang, D. Steering hollow multishelled structures in photocatalysis: Optimizing surface and mass transport. *Adv. Mater.* **2020**, *32*, 2002556.

[21] Wei, Y. Z.; Wan, J. W.; Yang, N. L.; Yang, Y.; Ma, Y. W.; Wang, S. C.; Wang, J. Y.; Yu, R. B.; Gu, L.; Wang, L. H. et al. Efficient sequential harvesting of solar light by heterogeneous hollow shells with hierarchical pores. *Natl. Sci. Rev.* **2020**, *7*, 1638–1646.

[22] Xin, Y. N.; Huang, Y.; Lin, K.; Yu, Y. F.; Zhang, B. Self-template synthesis of double-layered porous nanotubes with spatially separated photoredox surfaces for efficient photocatalytic hydrogen production. *Sci. Bull.* **2018**, *63*, 601–608.

[23] Xing, M. Y.; Qiu, B. C.; Du, M. M.; Zhu, Q. H.; Wang, L. Z.; Zhang, J. L. Spatially separated CdS shells exposed with reduction surfaces for enhancing photocatalytic hydrogen evolution. *Adv. Funct. Mater.* **2017**, *27*, 1702624.

[24] Zhang, P.; Luan, D. Y.; Lou, X. W. Fabrication of CdS frame-in-cage particles for efficient photocatalytic hydrogen generation under visible-light irradiation. *Adv. Mater.* **2020**, *32*, 2004561.

[25] Huang, L.; Wang, X. L.; Yang, J. H.; Liu, G.; Han, J. F.; Li, C. Dual cocatalysts loaded type I CdS/ZnS core/shell nanocrystals as effective and stable photocatalysts for H₂ evolution. *J. Phys. Chem. C* **2013**, *117*, 11584–11591.

[26] Xie, Y. P.; Yu, Z. B.; Liu, G.; Ma, X. L.; Cheng, H. M. CdS–mesoporous ZnS core–shell particles for efficient and stable photocatalytic hydrogen evolution under visible light. *Energy Environ. Sci.* **2014**, *7*, 1895–1901.

[27] Jiang, D. C.; Sun, Z. J.; Jia, H. X.; Lu, D. P.; Du, P. W. A cocatalyst-free CdS nanorod/ZnS nanoparticle composite for high-performance visible-light-driven hydrogen production from water. *J. Mater. Chem. A* **2016**, *4*, 675–683.

[28] Ran, J. R.; Zhang, J.; Yu, J. G.; Jaroniec, M.; Qiao, S. Z. Earth-abundant cocatalysts for semiconductor-based photocatalytic water splitting. *Chem. Soc. Rev.* **2014**, *43*, 7787–7812.

[29] Yin, Y. G.; Wei, S. T.; Zhang, L.; Guo, Z. W.; Huang, H. H.; Sai, S. R.; Wu, J. D.; Xu, Y. C.; Liu, Y.; Zheng, L. R. et al. Copper-linked 1T MoS₂/Cu₂O heterostructure for efficient photocatalytic hydrogen evolution. *Chem. Res. Chin. Univ.* **2020**, *36*, 1122–1127.

[30] Chang, K.; Hai, X.; Ye, J. H. Transition metal disulfides as noble-metal-alternative co-catalysts for solar hydrogen production. *Adv. Energy Mater.* **2016**, *6*, 1502555.

[31] Hinnemann, B.; Moses, P. G.; Bonde, J.; Jørgensen, K. P.; Nielsen, J. H.; Horch, S.; Chorkendorff, I.; Nørskov, J. K. Biomimetic hydrogen evolution: MoS₂ nanoparticles as catalyst for hydrogen evolution. *J. Am. Chem. Soc.* **2005**, *127*, 5308–5309.

[32] Chang, K.; Mei, Z. W.; Wang, T.; Kang, Q.; Ouyang, S. X.; Ye, J. H. MoS₂/graphene cocatalyst for efficient photocatalytic H₂ evolution under visible light irradiation. *ACS Nano* **2014**, *8*, 7078–7087.

[33] Xie, J. F.; Zhang, J. J.; Li, S.; Grote, F.; Zhang, X. D.; Zhang, H.; Wang, R. X.; Lei, Y.; Pan, B. C.; Xie, Y. Controllable disorder engineering in oxygen-incorporated MoS₂ ultrathin nanosheets for efficient hydrogen evolution. *J. Am. Chem. Soc.* **2013**, *135*, 17881–17888.

[34] Li, R. C.; Yang, L. J.; Xiong, T. L.; Wu, Y. S.; Cao, L. D.; Yuan, D. S.; Zhou, W. J. Nitrogen doped MoS₂ nanosheets synthesized via a low-temperature process as electrocatalysts with enhanced activity for hydrogen evolution reaction. *J. Power Sources* **2017**, *356*, 133–139.

[35] Xin, X.; Song, Y. R.; Guo, S. H.; Zhang, Y. Z.; Wang, B. L.; Wang, Y. J.; Li, X. H. One-step synthesis of P-doped MoS₂ for efficient photocatalytic hydrogen production. *J. Alloys Compd.* **2020**, *829*, 154635.

[36] Shi, Y.; Zhou, Y.; Yang, D. R.; Xu, W. X.; Wang, C.; Wang, F. B.; Xu, J. J.; Xia, X. H.; Chen, H. Y. Energy level engineering of MoS₂ by transition-metal doping for accelerating hydrogen evolution reaction. *J. Am. Chem. Soc.* **2017**, *139*, 15479–15485.

[37] Xie, J. F.; Zhang, H.; Li, S.; Wang, R. X.; Sun, X.; Zhou, M.; Zhou, J. F.; Lou, X. W.; Xie, Y. Defect-rich MoS₂ ultrathin nanosheets with additional active edge sites for enhanced electrocatalytic hydrogen evolution. *Adv. Mater.* **2013**, *25*, 5807–5813.

[38] Chen, D. Y.; Ji, G.; Ding, B.; Ma, Y.; Qu, B. H.; Chen, W. X.; Lee, J. Y. *In situ* nitrogenated graphene-few-layer WS₂ composites for fast and reversible Li⁺ storage. *Nanoscale* **2013**, *5*, 7890–7896.

[39] Gopannagari, M.; Kumar, D. P.; Reddy, D. A.; Hong, S.; Song, M. I.; Kim, T. K. *In situ* preparation of few-layered WS₂ nanosheets and exfoliation into bilayers on CdS nanorods for ultrafast charge carrier migrations toward enhanced photocatalytic hydrogen production. *J. Catal.* **2017**, *351*, 153–160.

[40] Lin, H. F.; Sun, B. W.; Wang, H.; Ruan, Q. Q.; Geng, Y. L.; Li, Y. Y.; Wu, J. K.; Wang, W. J.; Liu, J.; Wang, X. Unique 1D Cd₁₋ₓZnₓS@O-MoS₂/NiOₓ nano-hybrids: Highly efficient visible-light-driven photocatalytic hydrogen evolution via integrated structural regulation. *Small* **2019**, *15*, 1804115.

[41] Liu, L.; Jiao, Y.; Guo, Q.; Zhao, W.; Dai, W.; Zhang, J.; Gao, C.; Yu, W.; Li, X. Influence of sodium citrate on deposition and properties of Cd₁₋ₓZnₓS buffer layers by chemical bath deposition. *Chalcogenide Lett.* **2017**, *14*, 373–380.

[42] Sun, X. S.; Luo, X.; Zhang, X. D.; Xie, J. F.; Jin, S.; Wang, H.; Zheng, X. S.; Wu, X. J.; Xie, Y. Enhanced superoxide generation on defective surfaces for selective photooxidation. *J. Am. Chem. Soc.* **2019**, *141*, 3797–3801.

[43] Cai, L.; He, J. F.; Liu, Q. H.; Yao, T.; Chen, L.; Yan, W. S.; Hu, F. C.; Jiang, Y.; Zhao, Y. D.; Hu, T. D. et al. Vacancy-induced ferromagnetism of MoS₂ nanosheets. *J. Am. Chem. Soc.* **2015**, *137*, 2622–2627.

[44] He, Q.; Wan, Y. Y.; Zhang, Y. K.; Jiang, H. L.; Liu, H. J.; Zheng, X. S.; Chen, S. M.; Wu, X. J.; Song, L. 1T'-Mo₁₋ₓWₓS₂/CdS heterostructure enabling robust photocatalytic water splitting: Unveiling the interfacial charge polarization. *Solar RRL* **2018**, *2*, 1800032.

[45] Hao, X. Q.; Wang, Y. C.; Zhou, J.; Cui, Z. W.; Wang, Y.; Zou, Z. G. Zinc vacancy-promoted photocatalytic activity and photostability of ZnS for efficient visible-light-driven hydrogen evolution. *Appl. Catal. B Environ.* **2018**, *221*, 302–311.

[46] Lu, K. Q.; Qi, M. Y.; Tang, Z. R.; Xu, Y. J. Earth-abundant MoS₂ and cobalt phosphate dual cocatalysts on 1D CdS nanowires for boosting photocatalytic hydrogen production. *Langmuir* **2019**, *35*, 11056–11065.

[47] Zhang, Z.; Ma, X. X.; Tang, J. L. Porous NiMoO₄₋ₓ/MoO₂ hybrids as highly effective electrocatalysts for the water splitting reaction. *J. Mater. Chem. A* **2018**, *6*, 12361–12369.

[48] Sui, L. L.; Zhang, X. F.; Cheng, X. L.; Wang, P.; Xu, Y. M.; Gao, S.; Zhao, H.; Huo, L. H. Au-loaded hierarchical MoO₃ hollow spheres with enhanced gas-sensing performance for the detection of BTX (benzene, toluene, and xylene) and the sensing mechanism. *ACS Appl. Mater. Interfaces* **2017**, *9*, 1661–1670.

[49] Zhang, L. L.; Zhang, H. W.; Jiang, C. K.; Yuan, J.; Huang, X. Y.; Liu, P.; Feng, W. H. Z-scheme system of WO₃@MoS₂/CdS for photocatalytic evolution H₂: MoS₂ as the charge transfer mode switcher, electron-hole mediator and cocatalyst. *Appl. Catal. B Environ.* **2019**, *259*, 118073.

[50] Zhu, S. M.; Zhang, Y. A.; Qian, X. J.; Wang, X. X.; Su, W. Y. Zn defect-mediated Z-scheme electron-hole separation in AgIn₅S₈/ZnS heterojunction for enhanced visible-light photocatalytic hydrogen evolution. *Appl. Surf. Sci.* **2020**, *504*, 144396.

[51] Zhou, P. S.; Xu, Q.; Li, H. X.; Wang, Y.; Yan, B.; Zhou, Y. C.; Chen, J. F.; Zhang, J. N.; Wang, K. X. Fabrication of two-dimensional lateral heterostructures of WS₂/WO₃·H₂O through selective oxidation of monolayer WS₂. *Angew. Chem., Int. Ed.* **2015**, *54*, 15226–15230.

[52] Ratcliff, E. L.; Meyer, J.; Steirer, K. X.; Garcia, A.; Berry, J. J.; Ginley, D. S.; Olson, D. C.; Kahn, A.; Armstrong, N. R. Evidence for near-surface NiOOH species in solution-processed NiOₓ selective interlayer materials: Impact on energetics and the performance of polymer bulk heterojunction photovoltaics. *Chem. Mater.* **2011**, *23*, 4988–5000.

[53] Guan, S. D.; Fu, X. L.; Zhang, Y.; Peng, Z. J. NiS modified CdS nanowires for photocatalytic H₂ evolution with exceptionally high efficiency. *Chem. Sci.* **2018**, *9*, 1574–1585.

[54] Vrubel, H.; Merki, D.; Hu, X. L. Hydrogen evolution catalyzed by MoS₃ and MoS₂ particles. *Energy Environ. Sci.* **2012**, *5*, 6136–6144.

[55] Chang, Y. H.; Lin, C. T.; Chen, T. Y.; Hsu, C. L.; Lee, Y. H.; Zhang, W. J.; Wei, K. H.; Li, L. J. Highly efficient electrocatalytic hydrogen production by MoSₓ grown on graphene-protected 3D Ni foams.

Adv. Mater. **2013**, *25*, 756–760.

[56] Xiong, J. H.; Liu, Y. H.; Wang, D. K.; Liang, S. J.; Wu, W. M.; Wu, L. An efficient cocatalyst of defect-decorated MoS$_2$ ultrathin nanoplates for the promotion of photocatalytic hydrogen evolution over CdS nanocrystal. *J. Mater. Chem. A* **2015**, *3*, 12631–12635.

[57] Zhu, Z. Z.; Li, X. X.; Qu, Y. T.; Zhou, F. Y.; Wang, Z. Y.; Wang, W. Y.; Zhao, C. M.; Wang, H. J.; Li, L. Q.; Yao, Y. G. et al. A hierarchical heterostructure of CdS QDs confined on 3D ZnIn$_2$S$_4$ with boosted charge transfer for photocatalytic CO$_2$ reduction. *Nano Res.* **2021**, *14*, 81–90.

[58] Kim, E. S.; Nishimura, N.; Magesh, G.; Kim, J. Y.; Jang, J. W.; Jun, H.; Kubota, J.; Domen, K.; Lee, J. S. Fabrication of CaFe$_2$O$_4$/TaON heterojunction photoanode for photoelectrochemical water oxidation. *J. Am. Chem. Soc.* **2013**, *135*, 5375–5383.

[59] Shen, R. C.; Ding, Y. N.; Li, S. B.; Zhang, P.; Xiang, Q. J.; Ng, Y. H.; Li, X. Constructing low-cost Ni$_3$C/twin-crystal Zn$_{0.5}$Cd$_{0.5}$S heterojunction/homojunction nanohybrids for efficient photocatalytic H$_2$ evolution. *Chin. J. Catal.* **2021**, *42*, 25–36.

[60] Zhuang, T. T.; Liu, Y.; Sun, M.; Jiang, S. L.; Zhang, M. W.; Wang, X. C.; Zhang, Q.; Jiang, J.; Yu, S. H. A unique ternary semiconductor-(semiconductor/metal) nano-architecture for efficient photocatalytic hydrogen evolution. *Angew. Chem., Int. Ed.* **2015**, *54*, 11495–11500.

[61] Xiang, X. M.; Chou, L. J.; Li, X. H. Synthesis of PdS-CdSe@CdS-Au nanorods with asymmetric tips with improved H$_2$ production efficiency in water splitting and increased photostability. *Chin. J. Catal.* **2018**, *39*, 407–412.

[62] Shen, J. X.; Li, Y. Z.; Zhao, H. Y.; Pan, K.; Li, X.; Qu, Y.; Wang, G. F.; Wang, D. S. Modulating the photoelectrons of g-C$_3$N$_4$ via coupling MgTi$_2$O$_5$ as appropriate platform for visible-light-driven photocatalytic solar energy conversion. *Nano Res.* **2019**, *12*, 1931–1936.

[63] Ran, J. R.; Gao, G. P.; Li, F. T.; Ma, T. Y.; Du, A. J.; Qiao, S. Z. Ti$_3$C$_2$ MXene co-catalyst on metal sulfide photo-absorbers for enhanced visible-light photocatalytic hydrogen production. *Nat. Commun.* **2017**, *8*, 13907.

[64] Liu, J. F.; Wang, P.; Fan, J. J.; Yu, H. G.; Yu, J. G. Hetero-phase MoC-Mo$_2$C nanoparticles for enhanced photocatalytic H$_2$-production activity of TiO$_2$. *Nano Res.* **2021**, *14*, 1095–1102.

[65] Chu, J. Y.; Han, X. J.; Yu, Z.; Du, Y. C.; Song, B.; Xu, P. Highly efficient visible-light-driven photocatalytic hydrogen production on CdS/Cu$_7$S$_4$/g-C$_3$N$_4$ ternary heterostructures. *ACS Appl. Mater. Interfaces* **2018**, *10*, 20404–20411.

[66] Ling, C. C.; Ye, X. J.; Zhang, J. H.; Zhang, J. F.; Zhang, S. J.; Meng, S. G.; Fu, X. L.; Chen, S. F. Solvothermal synthesis of CdIn$_2$S$_4$ photocatalyst for selective photosynthesis of organic aromatic compounds under visible light. *Sci. Rep.* **2017**, *7*, 27.

[67] Nowak, M.; Kauch, B.; Szperlich, P. Determination of energy band gap of nanocrystalline SbSI using diffuse reflectance spectroscopy. *Rev. Sci. Instrum.* **2009**, *80*, 046107.

[68] Li, S. S.; Wang, L.; Li, Y. D.; Zhang, L. H.; Wang, A. X.; Xiao, N.; Gao, Y. Q.; Li, N.; Song, W. Y.; Ge, L. et al. Novel photocatalyst incorporating Ni-Co layered double hydroxides with P-doped CdS for enhancing photocatalytic activity towards hydrogen evolution. *Appl. Catal. B Environ.* **2019**, *254*, 145–155.